Cell Reports
Physical Science

CellPress
OPEN ACCESS

Article

Integration of low-melting-point alloys and thermoplastic elastomers for 3D printing of multifunctional composites

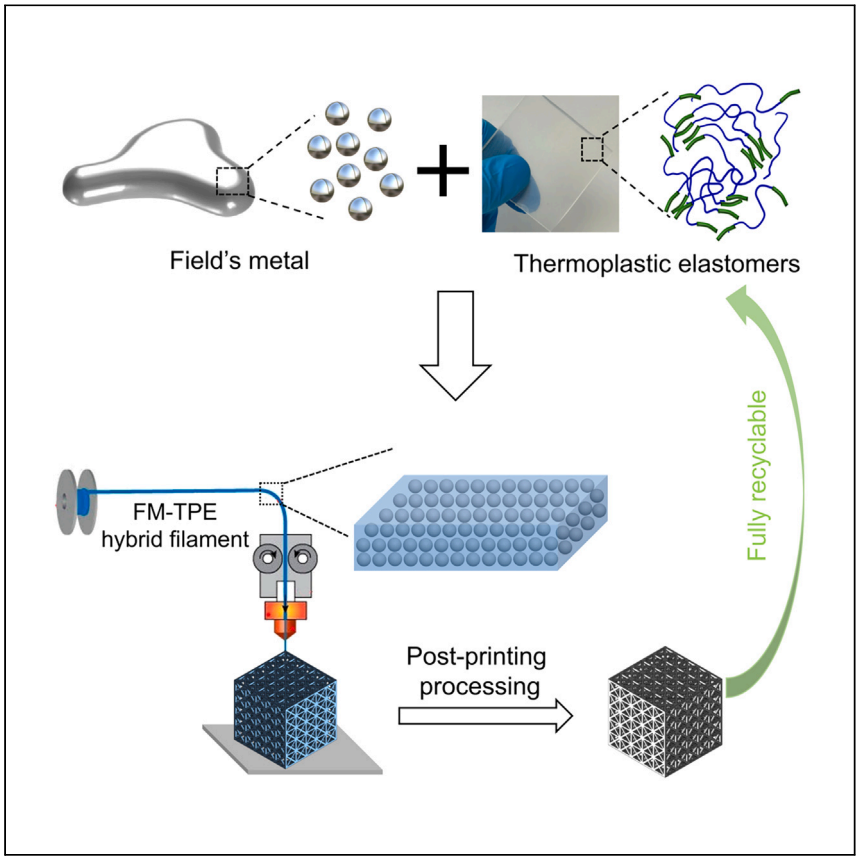

Metal 3D printing generally requires high energy and/or high temperature, which are energy intensive and not compatible with polymers. Here, Bu et al. report a 3D-printable material platform by integrating Field's metal and thermoplastic elastomers in a synergistic way, applicable for various metal-polymer and metal-carbon composites.

Jinyu Bu, Naifu Shen, Zhao Qin, Weinan Xu

zqin02@syr.edu (Z.Q.)
weinanxu@uakron.edu (W.X.)

Highlights

A 3D-printable polymer-metal composite material platform is developed

Integration of Field's metal and thermoplastic elastomers enables fine structural control

Fused filament fabrication of 3D structures with the composite is demonstrated

Post-printing processing generates conductive pathways and fully inorganic structures

Bu et al., Cell Reports Physical Science 4, 101604
October 18, 2023
https://doi.org/10.1016/j.xcrp.2023.101604

Cell Reports
Physical Science

CellPress
OPEN ACCESS

Article

Integration of low-melting-point alloys and thermoplastic elastomers for 3D printing of multifunctional composites

Jinyu Bu,[1] Naifu Shen,[1] Zhao Qin,[2,*] and Weinan Xu[1,3,*]

SUMMARY

Due to the significant differences in the physical and chemical properties of polymers and metals, their additive manufacturing is conducted using very different and incompatible methods or conditions. Such incompatibility is a significant limitation for multimaterial 3D printing and fabrication of 3D functional composites. We address this issue by creating functional composites composed of thermoplastic elastomers, Field's metal, and graphene; and their 3D printability by fused filament fabrication is achieved. The fully recyclable 3D-printable composites are featured with widely tunable internal structures and mechanical, thermal, and electrical properties. Multiphysics modeling is further developed to elucidate the structure-property relationship. The 3D structures can be transformed from insulative to conductive based on the melting and coalescence of Field's metal nanoparticles. The incorporation of graphene bridges the adjacent Field's metal particles and significantly enhances conductivity. Such 3D-printable polymer-metal hybrid platform could enable advancements in soft electronics and robotics and in energy storage.

INTRODUCTION

Additive manufacturing of polymers, metals, and their composites has been at the forefront of manufacturing and materials research in recent decades.[1–3] Compared with traditional manufacturing, additive manufacturing or 3D printing is easy to customize, is capable of fabricating complex geometries, has lower tooling costs, and generates less material waste.[4,5] The application of 3D printing in various fields has started to revolutionize the manufacturing of medical devices, automotive/aerospace components, sports equipment, and construction projects.[6–9]

Polymers and metals are the two most important types of materials in additive manufacturing. Due to the significant differences in the physical and chemical properties of metals and polymers, 3D printing of the two types of materials is conducted using very different and incompatible methods or conditions.[4,10] The 3D printing technologies commonly used for polymers (which have relatively low softening or melting temperatures) include extrusion-, resin-, and powder-based methods.[11–13] Of these, extrusion-based methods, especially fused filament fabrication (FFF), are widely used due to their low costs and the broad selection of compatible polymers.[10,13,14] FFF involves layer-by-layer extrusion through a heated nozzle of a polymer filament, which cools and solidifies on the printing bed.[15] In contrast, the 3D printing of metals generally utilizes quite different methods and conditions, such as powder bed fusion, binder jetting, and direct energy deposition,[16,17] which

[1]School of Polymer Science and Polymer Engineering, The University of Akron, Akron, OH 44325, USA

[2]Department of Civil and Environmental Engineering, Syracuse University, Syracuse, NY 13244, USA

[3]Lead contact

*Correspondence: zqin02@syr.edu (Z.Q.), weinanxu@uakron.edu (W.X.)

https://doi.org/10.1016/j.xcrp.2023.101604

generally involve the use of a high-energy laser or an electron beam to sinter or melt the metal particles into 3D parts.[18]

The incompatibility of additive manufacturing processes and conditions for polymers and metals is a significant limitation for multimaterial 3D printing and the fabrication of polymer-metal composite structures. There are recent research endeavors to integrate metals and polymers in the FFF 3D printing process for fabricating metallic 3D structures. However, simple blending of metallic particles (such as iron or bronze) with thermoplastics for FFF 3D printing without sintering results in decreased printability and poor mechanical properties compared with pristine polymers.[19–21] Metal FFF and bound metal deposition technologies, which are based on metal injection molding, have also been developed.[22–24] For instance, filaments containing stainless steel powder (80–90 wt %) mixed with polyacetal and polyolefin can be used for FFF, and the 3D-printed objects require post-processing and sintering at high temperatures to obtain the final parts. However, this approach has several major limitations, including the following: (1) high-temperature sintering (1,380°C) required after printing is energy and cost intensive; (2) large and anisotropic deformation during the sintering process (20% or more) limits the fabrication precision; (3) a debinding process that employs harsh chemicals needs be performed before the parts can be sintered; and (4) specialized equipment is required for the debinding and sintering of the printed parts.

Compared with those recently developed metal FFF 3D printing technologies, the fabrication of continuous 3D metallic or composite structures that can be fully recycled and without the need for high-temperature sintering will have significant advantages due to the ease of fabrication, energy savings, and lower carbon emissions. To achieve this objective, it is necessary to utilize metals or alloys with melting points (T_m) that are within the regular printing temperatures used in FFF technology (i.e., 250°C or lower).

The most intensively studied metals with low T_m are gallium-based liquid metals such as EGaIn (a eutectic alloy of gallium and indium) and Galinstan (an alloy of gallium, indium, and tin).[25–28] As their T_m values are below room temperature, these alloys can be easily extruded with pressure into a mold or channel.[29,30] Also, the formation of an ultrathin oxide layer on the surface helps to stabilize structures made from gallium-based liquid metals.[31–33] There are quite a few recent reports on 3D printing with liquid metals or their composites.[34–38] However, the low T_m (below room temperature) also brings significant limitations to their 3D printing because the 3D-printed structure is unable to stably maintain its complex geometry without a support matrix.[39–42] Another major limitation in using gallium and its alloys for additive manufacturing is their corrosive nature to most other metals,[25] which leads to severe damage to the metallic components of 3D printers and related equipment.

Compared with those liquid metals, several important types of low-melting-point alloys (LMPAs) have T_m values that are above room temperature, and most contain bismuth (Bi); examples are Rose's metal, Wood's metal, and Field's metal (FM).[43] Of these, FM (a eutectic alloy of bismuth, indium, and tin) stands out as an ideal candidate for additive manufacturing.[44,45] Its T_m of 62°C ensures stability under ambient conditions and melt processability under FFF 3D-printing conditions. Moreover, it does not contain toxic elements such as lead, and it is not corrosive to most other metals. There is increasing interest in FM for nanotechnology and advanced fabrication beyond its conventional use in die casting and prototyping.[31,46,47] However, FM itself is not suitable for extrusion-based 3D printing due to its high rigidity and

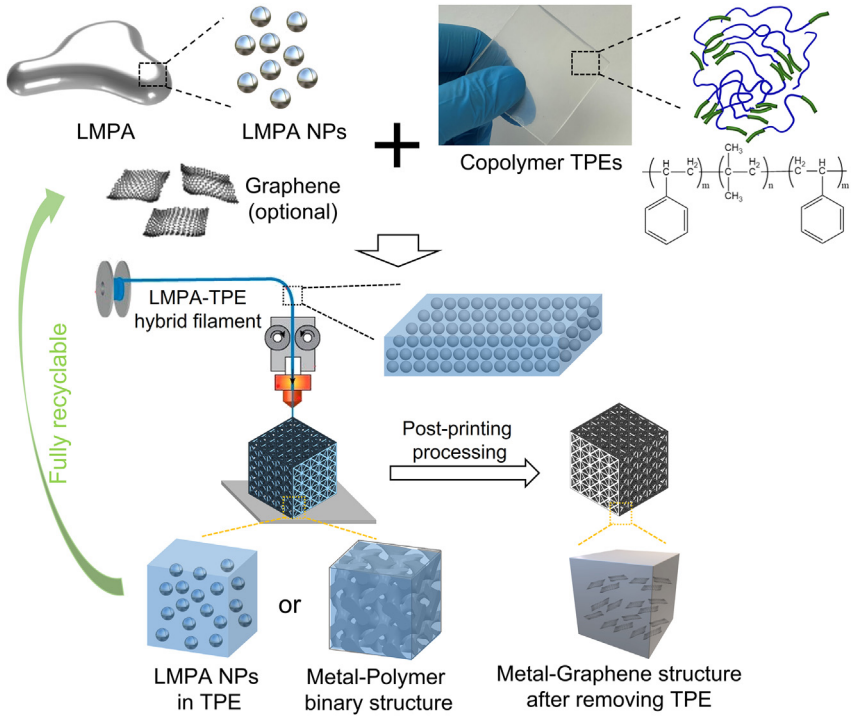

Figure 1. Schematic illustration of the hybrid material system and 3D printing

(Top) Schematic and chemical structure of LMPA NPs, copolymer TPE, and graphene used in this study. (Bottom) FFF 3D printing with LMPA-TPE hybrid filaments to fabricate 3D polymer-metal composites with widely tunable internal structures. The printed structures can be fully recycled into the original components.

modulus (9.25 GPa) at room temperature, as well as its unsuitable rheological properties (low viscosity and non-thixotropic) in its melt state.[48]

To overcome these issues, in this study, we create LMPA nanostructures and integrate them with a soft and flexible thermoplastic elastomer (TPE) matrix. TPE is a type of block copolymer with the excellent processability of a thermoplastic and the high elasticity of an elastomer.[49,50] The FM-TPE composites are successfully produced in filaments, and such hybrid filaments are used for FFF 3D printing into various 3D structures with highly tunable internal structures and physical properties. Multiphysics modeling is developed to theoretically elucidate the structure-property relationship. The temperature-induced melting and coalescence of FM nanoparticles (NPs) inside the TPE matrix are critical for the on-demand and reversible control of mechanical properties and electrical conductivity of the printed structures. Moreover, graphene is incorporated in some composites, which can bridge the FM NPs and create conductive pathways. It also enables the creation of 3D metal-graphene structures with excellent shape/size retention (97% and higher) when the TPE binder is removed by calcination. The 3D-printed composite structures can be easily recycled into separate FM and TPE for new printing and reduce the overall cost.

RESULTS AND DISCUSSION

Hybrid material system for 3D printing

In our hybrid material system, the two major components are LMPA NPs and TPE, with the option to further incorporate graphene (Figure 1). The LMPA, such as FM NPs, can be conveniently fabricated by probe sonication of bulk FM in solution.

The TPE used in our study is polystyrene-*b*-polyisobutylene-*b*-polystyrene (SIBS), with the chemical structure shown in Figure 1. SIBS was chosen as the soft matrix for the following reasons: (1) its thermal processability and high stability enable FFF printability and recyclability; (2) its high elasticity enables the LMPA-TPE composites to be potentially conductive and stretchable; and (3) its well-defined and tunable molecular structure enables chemical functionalization when needed. It is noted that SIBS with high polyisobutylene (PIB) content (70% or higher) is too soft (Shore A 43 or lower) for consistent FFF 3D printing. We incorporated polystyrene (PS) homopolymer in SIBS (weight ratio of 1:1) to further enhance the printability as demonstrated in our previous studies.[51,52] In the following discussion, TPE is used to represent the SIBS/PS polymer matrix for simplicity. The FM-TPE composites with tunable composition and internal structures are used for FFF 3D printing (Figure 1); the morphology and properties of printed structures have strong dependence on the filament composition and post-printing processing, as will be discussed later. Importantly, the 3D-printed structures can be fully recycled into the original LMPA and TPE components for sustainable manufacturing and reducing cost.

Properties of FM NPs and TPE

FM NPs were prepared by probe sonication of bulk FM in toluene in the presence of small organic ligands (1-dodecanethiol), and the temperature of the solution (70°C) was above the T_m of FM. The organic ligands are necessary to achieve relatively small size and narrow size distribution of FM NPs. A scanning electron microscopy (SEM) image (Figure 2A) shows that the FM NPs are special in shape and have sizes in the range of 150–400 nm. Dynamic light scattering (DLS) data (Figure 2B) further show that the average hydrodynamic diameter of the FM NPs is about 250 nm. The size distribution can be further improved by purification with step centrifugation. The dimension of the FM NPs plays an important role in their interactions with the TPE copolymer matrix. An average size of below 500 nm is needed to achieve their uniform dispersion within the soft matrix. The presence of organic ligands and oxide shells on the surface of the FM NPs also affects their coalescence during their printing and processing,[53–55] as will be discussed in a later section.

Differential scanning calorimetry (DSC) study (Figure 2C) of bulk FM confirms its T_m at 62°C and a solidification temperature (T_s) during the cooling cycle of 57°C. For the FM NPs, the melting point remains at 62°C. However, due to the size-induced undercooling effects,[44,56] the solidification point shifts to lower temperatures, with two peaks at 35°C and 26°C. The TPE matrix used in this study, SIBS, has a typical microphase-separated morphology between the PS and the PIB blocks, forming PS cylinders dispersed in the PIB matrix, as shown in the atomic force microscope (AFM) image (Figure 2D). The TPE matrix has two glass transition temperatures, one is for the PIB block at around −60°C, and the other is for the PS block at around 96°C (Figure S1).

Fabrication and characterization of the FM-TPE composites

The FM NPs and TPE were blended in toluene to form a homogeneous solution, and then the solvent was evaporated to obtain composite films. Such FM-TPE composite films were then cut into small pieces and fed into a desktop extruder to fabricate composite filaments for FFF 3D printing. Representative images of the filaments are shown in Figures 3A–3D. The filaments have a uniform diameter of 1.75 mm, mechanical flexibility, and a smooth surface. It is noted that the dark color of the filaments is due to the strong light scattering of FM NPs inside the filament. Cross-section SEM (Figure 3D) of 50 wt % FM-TPE filament clearly shows that the high density of FM NPs is uniformly distributed inside the polymer matrix.

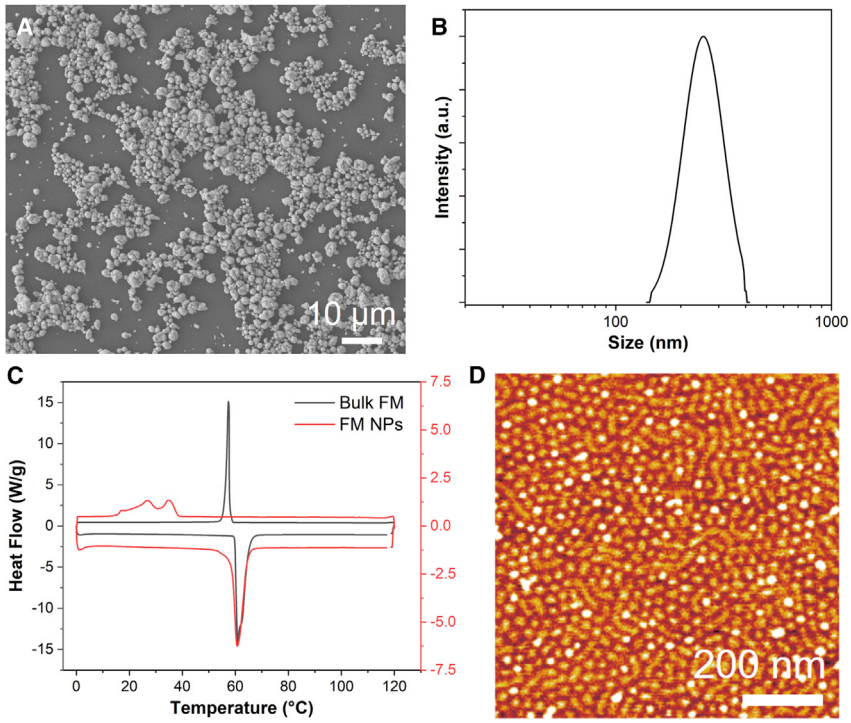

Figure 2. Characterization of FM NPs and TPE matrix

(A) SEM image of FM NPs prepared by probe sonication.

(B) DLS curve of the FM NP dispersion in a solvent.

(C) DSC curves for bulk FM and FM NPs.

(D) AFM phase image of the SIBS copolymer TPE showing microphase separated morphology. Scale bars, 10 μm (A) and 200 nm (D).

The internal structure of FM-TPE composites and its dependence on the metal-to-polymer ratio are theoretically investigated with a phase-field model. This model simulates the structure evolution of two mutually exclusive melts of different volume fractions and of initially uniform spatial distribution by numerically solving the Cahn-Hilliard equation and visualizing the separation of the two phases (more details in Figures S2 and S3).[57,58] Figure 3E shows the internal structure of the FM-TPE composites with different FM contents (3Ei, 50 wt %; 3Eii, 70 wt %; 3Eiii, 80 wt %; 3Eiv, 90 wt %) in the stable state predicted from the phase-field modeling. It can be seen that with the increase in FM loading, a higher density of larger metal particles is generated from the coalescence of smaller FM NPs. When the FM weight fraction exceeds 90 wt %, the FM and TPE spontaneously form a bicontinuous structure. It is noted that the phase-field modeling is applied under the condition that both TPE and FM are in the melt state for a sufficiently long time, which has differences with the experimental FM-TPE composite fabrication within a finite time, but the general trends in internal structure evolution match well with each other (see also Figure S4).

To study the thermal stability and validate the weight percentage of FM NPs inside the composite filaments, thermogravimetric analysis (TGA) was performed (Figure 3F). For the FM-TPE filaments, the thermal degradation started at around 370°C, and the maximum degradation rate occurred at around 440°C. The residual weight at 500°C and higher corresponds to the amount of FM NPs in the composites. For the FM-TPE composites prepared with 70 and 80 wt % FM, the residual weights

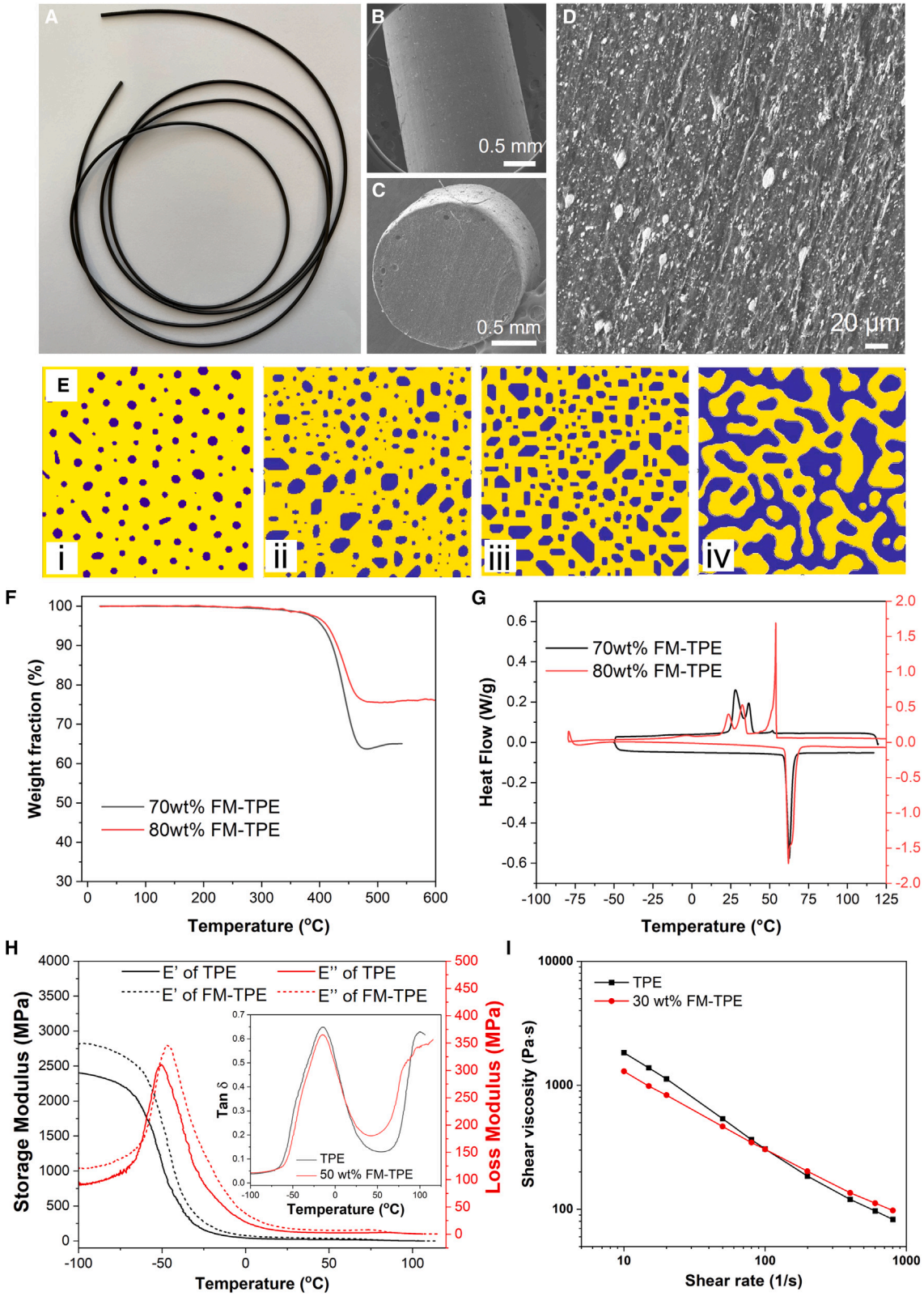
A
B
0.5 mm
C
0.5 mm
D
20 μm
E
i
ii
iii
iv
F
Weight fraction (%)
Temperature (°C)
70wt% FM-TPE
80wt% FM-TPE
G
Heat Flow (W/g)
Temperature (°C)
70wt% FM-TPE
80wt% FM-TPE
H
Storage Modulus (MPa)
Loss Modulus (MPa)
Temperature (°C)
E' of TPE
E'' of TPE
E' of FM-TPE
E'' of FM-TPE
Tan δ
TPE
50 wt% FM-TPE
I
Shear viscosity (Pa·s)
Shear rate (1/s)
TPE
30 wt% FM-TPE

Figure 3. Preparation and characterization of the FM-TPE composites

(A) Photo of the FM-TPE filament.

(B–D) SEM images of the surface (B) and cross section (C and D) of a 50 wt % FM-TPE filament.

(E) The internal structure of FM (blue)-TPE (yellow) composites with different FM contents (i, 50 wt %; ii, 70 wt %; iii, 80 wt %; iv, 90 wt %) generated from the phase-field modeling. The simulation box size is 95 by 95 μm.

(F) TGA curves of FM-TPE composites with 70 and 80 wt % FM.

(G) DSC curves of the FM-TPE composites with 70 and 80 wt % FM.

(H) DMA characterization including storage and loss modulus of the 50 wt % FM-TPE and TPE samples. Inset shows the damping (tan δ) of the same samples.

(I) Shear viscosity as a function of shear rate for 30 wt % FM-TPE sample. Scale bars, 0.5 mm (B and C) and 20 μm (D).

are about 65% and 76%, respectively, which confirms the composition of the composite filaments.

DSC characterization was conducted on the FM-TPE composites with 70 and 80 wt % FM (Figure 3G). The main peaks all originate from FM NPs and the glass transition of the TPE matrix has a much lower intensity. The melting peaks for FM NPs appear at 62°C for both samples. The solidification peaks for the 70 wt % FM-TPE composite appear at 36°C and 28°C, which is due to size-induced undercooling and consistent with pristine FM NPs. Interestingly, for the 80 wt % FM-TPE composite, in addition to the two undercooled solidification peaks at 32°C and 23°C, there is also another solidification peak at 54°C, which is close to the T_s of bulk FM. This indicates that, when the FM NP loading is close to or exceeds 80 wt %, some of the FM NPs can coalesce and form relatively large metal structures in the polymer matrix during filament fabrication. This is confirmed by SEM images of the filament cross section as shown in Figure S4.

Dynamic mechanical analysis (DMA) was used to study the thermomechanical properties of the FM-TPE composites (Figure 3H). With the incorporation of FM NPs, the 50 wt % FM-TPE has substantially higher storage and loss modulus at temperatures below the T_m of FM (62°C) due to the reinforcement effect of rigid FM NPs. When temperature increases to close to and above the T_m of FM, the composite and pristine TPEs have very close modulus values. From the damping curves (Figure 3H, inset), it can be seen that pristine TPE has two major transitions, a high-temperature transition, corresponding to the glass transition (T_g) of the PS at ~100°C, and a low-temperature transition consisting of a shoulder at −40°C associated with the PIB block and a strong peak at −15°C due to a sub-Rouse-type motion caused by relaxation at longer time scales.[59,60] For the 50 wt % FM-TPE composite, in addition to the transitions mentioned above, it has a shoulder peak at around 65°C, which is due to the melting transition of FM NPs at this temperature range.

Another important parameter for successful FFF 3D printing is the shear viscosity at printing temperature, which can be measured by a capillary rheometer. The shear viscosity of the melt needs to be in a suitable range because too-high shear viscosity leads to difficulty in extrusion from the nozzle, and too-low shear viscosity leads to overextrusion. The shear viscosity as a function of shear rate at a temperature of 230°C for the pristine TPE and 30 wt % FM-TPE is shown in Figure 3I. Both samples show shear-thinning behavior. The shear viscosity at a shear rate of 20 s^{-1}, which correspond to a printing speed of ~2 mm s^{-1} (details of the shear rate calculation are in the supplemental information), is 1,125 and 832 Pa s for the pristine TPE and 30 wt % FM-TPE, respectively. Both values are within the suitable range for FFF 3D printing.

Also, the results show that FM-TPE has a lower shear viscosity than pristine TPE at low shear rates (below 100 s^{-1}), but higher than it at higher shear rates, The possible mechanism is that, in the high-shear-rate region, the FM NPs are better dispersed,

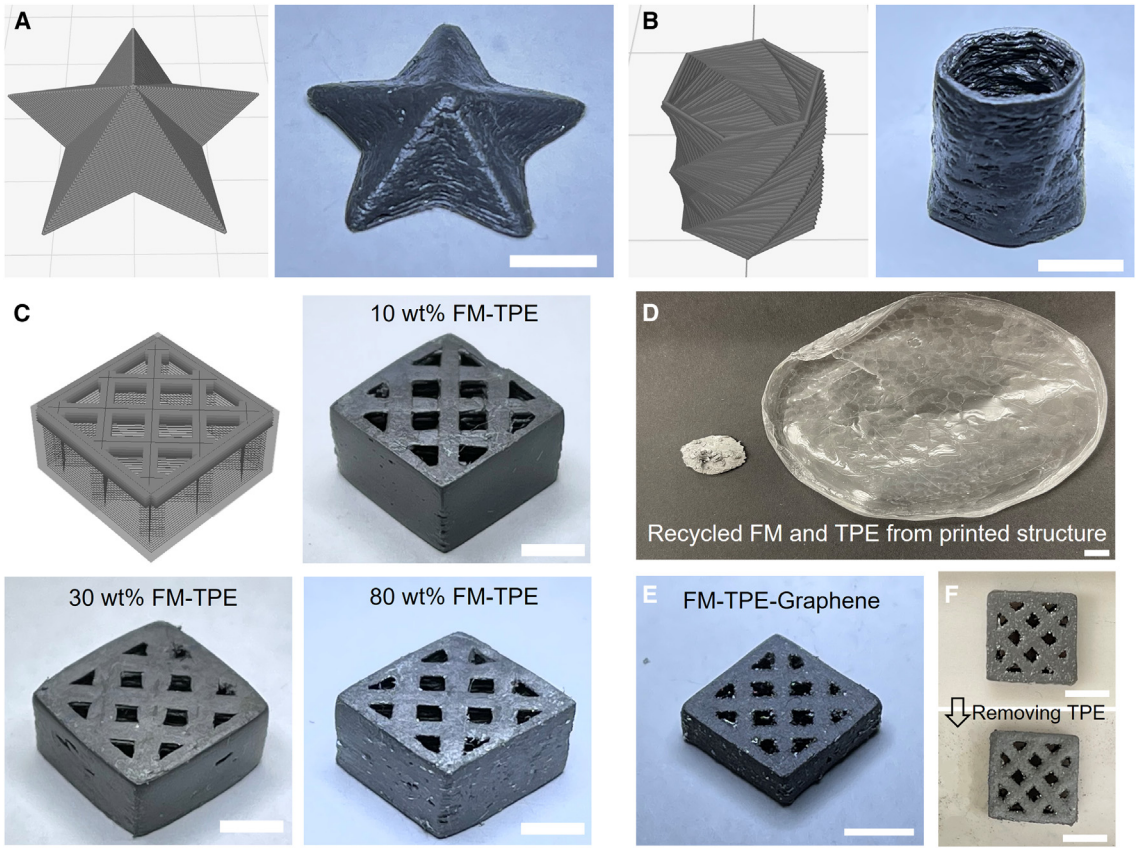

Figure 4. Representative 3D-printed samples from FM-TPE composite filaments

(A and B) Star and twisted cylinder printed from 10 wt % FM-TPE composite filament. On the left is the 3D model, and on the right is the photo of the printed structure.

(C) Comparison of the printing quality of the same infill-patterned cubes using three different composite filaments: 10 wt % FM-TPE, 30 wt % FM-TPE, and 80 wt % FM-TPE.

(D) Recycling of a 3D-printed cube of 80 wt % FM-TPE into its original components: FM and TPE.

(E) 3D-printed cube with infill patten from FM-TPE-graphene filament (80 wt % FM and 10% graphene).

(F) Conversion of the 3D-printed FM-TPE-graphene structure to metal-graphene composite with excellent shape retention. All scale bars, 5 mm.

and the FM-TPE composite is similar to conventional polymer nanocomposites with sub-microparticles, whose viscosity is higher than that of pristine polymers. This is consistent with many previous studies on the rheological properties of polymer nanocomposites.[61] In the low-shear-rate regime, the FM NPs are expected to have more local coalescence,[62] and the FM melt has a lower viscosity compared with the TPE melt. Therefore, the overall shear viscosity is reduced due to the existence of large low-viscosity domains in the polymer matrix, the detailed mechanism of which will be systematically investigated in a future study.

FFF 3D printing with FM-TPE composites

With the elucidation of the physical properties of the FM-TPE composites, the filaments were then used for the fabrication of 3D structures via FFF 3D printing. Figures 4A and 4B show a 3D-printed star and twisted cylinder from a 10 wt % FM-TPE filament. It can be seen that the shape fidelity is high (within 3% difference compared with the digital model) and the surface is relatively smooth. We also investigated and compared the printability of FM-TPE composites with different FM contents. Figure 4C shows the same cubic structure with infill patterns printed

from FM-TPE filament with 10, 30, and 80 wt % FM. In this composition range, all of the composites show reasonably high printability. The surface roughness slightly increases with increasing FM content. It is also noted that, for the 3D-printed 80 wt % FM-TPE composite, there are some shiny metallic spots on the structure, which are due to the coalescence of FM particles at high concentrations during printing.

Another unique advantage of our FM-TPE composite system is its full recyclability. The 3D-printed FM-TPE composite structures can be dissolved in an organic solvent (such as toluene). The metal NPs will precipitate and separate from the polymer solution, while the TPE can be recovered after the solvent is evaporated. We demonstrated the recycling of an infill-patterned cube printed from 80 wt % FM-TPE filament. After the recycling, the separated FM and TPE film are shown in Figure 4D. Weight measurements and comparison indicate that both the FM and the TPE can be recovered at 99.1% or higher of their original amount. Those recycled FM and TPE can be reprocessed into composite filaments for new 3D printing.

Importantly, due to the presence of a thin oxide shell on the surface of FM NPs and the insulative nature of the TPE, the FM-TPE composite structures have low conductivity in the as-printed state even at high FM content (such as 80 wt %). To address this issue and bring additional functionality to the composites, we incorporated graphene into some of the FM-TPE composites. For instance, we prepared FM-TPE-graphene composites (80 wt % FM and 10% graphene) by a similar solution blending and then used the composite filament to 3D print a cube with infill pattern (Figure 4E).

The FM-TPE-graphene composite maintains high FFF printability with some coalesced FM particles visible on the surface. Moreover, such 3D-printed FM-TPE-graphene structures can be converted into fully inorganic metal-graphene composite structures (Figure 4F) with excellent shape and size retention (with dimensional shrinkage of less than 4%). This is much better than conventional metal FFF 3D printing, where the size shrinkage is usually 15%–20% or higher during post-printing processing. Such 3D metal-graphene composite structures are ideal candidates for energy storage and electronics applications.

The internal structure of the 3D-printed FM-TPE composites was studied by cross-section SEM and energy-dispersive X-ray spectroscopy (EDX) analysis. Figures 5A–5C show the cross-section morphology of the 3D-printed samples with three different FM NP loadings: 50, 70, and 80 wt %. It can be seen that the 50 wt % FM-TPE sample has uniformly dispersed FM NPs with relatively small size (<1 μm) in the TPE matrix. For the 3D-printed 70 wt % FM-TPE structure, some larger FM particles (tens of micrometers) due to local coalescence start to appear. When the FM loading further increases to 80 wt %, more coalesced large FM particles appear, and a few defects can also be observed.

For the 3D-printed FM-TPE-graphene (80 wt % FM and 10 wt % graphene) composites (Figure 5D), the TPE now acts as a polymer binder for graphene and FM NPs. The FM NPs are intercalated by graphene nanosheets, which leads to significantly enhanced electrical and thermal conductivity, as will be discussed later. Furthermore, the interpenetrated metal-graphene structure enables excellent shape retention capability, as shown in Figure 4F. Without graphene, the as-printed FM-TPE structures are generally not able to maintain their integrity after the TPE is removed, due to the discrete FM NPs. Relatively high loading of FM NPs (80 wt %) is also important for excellent size and shape retention, as composites with higher volume fractions of TPE or lower FM loading are expected to lead to more shrinkage after TPE removal.

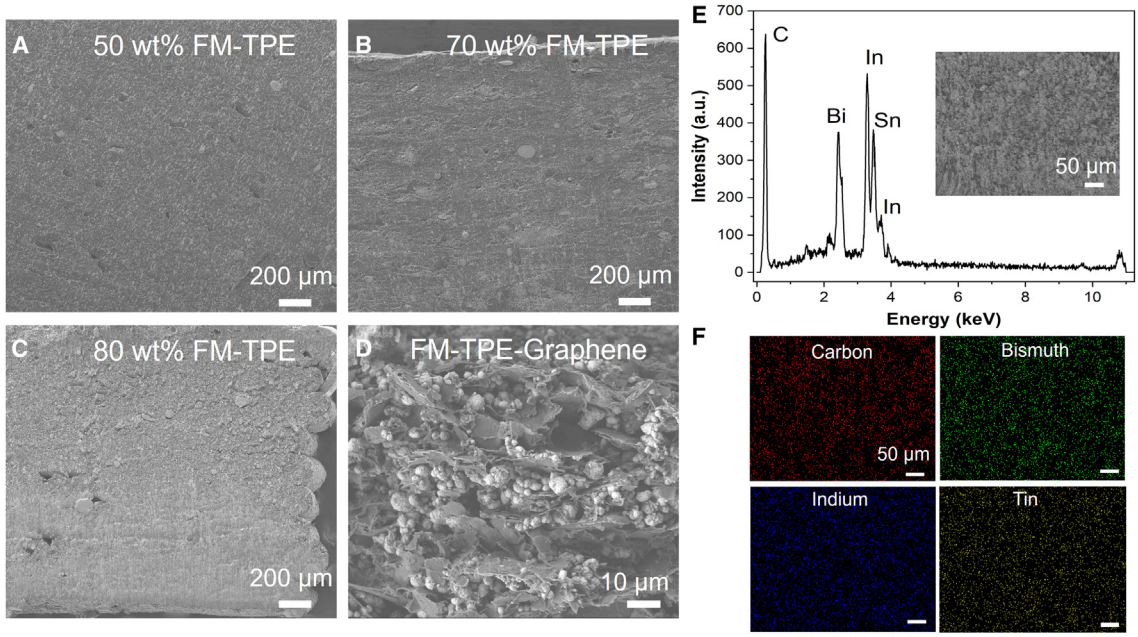

Figure 5. Internal structure characterization of the 3D-printed composite structures

(A–D) Cross-section SEM images of the 3D-printed structures from (A) 50 wt % FM-TPE, (B) 70 wt % FM-TPE, (C) 80 wt % FM-TPE, and (D) 80 wt % FM-TPE-graphene.

(E) EDX spectrum collected from the cross section of a 3D-printed 80 wt % FM-TPE structure; inset shows the SEM image of the measured area.

(F) The corresponding elemental mapping of the cross-section area (E inset) in the 3D-printed 80 wt % FM-TPE structure. Scale bars, 200 μm (A–C), 10 μm (D), and 50 μm (E and F).

The EDX spectrum (Figure 5E) obtained from the cross section of the 3D-printed 80 wt % FM-TPE structure clearly shows the characteristic peaks for carbon (0.26 keV), bismuth (2.42 keV), indium (3.29 and 3.70 keV), and tin (3.47 keV). Elemental mapping (Figure 5F) further confirms that the majority of the FM NPs are well dispersed in the polymer matrix without severe aggregation. Micro-computed tomography (micro-CT) was also used to study the internal structure and showed that FM NPs are uniformly dispersed inside the TPE matrix (Figure S5).

Transformation from insulative to conductive state by structural tuning

Another important property of the FM-TPE composites and their 3D-printed structures is their potentially high electrical conductivity. Bulk FM has high intrinsic electrical conductivity on the order of 10^5 S/m. However, due to the existence of an insulating oxide shell on the surface, FM NPs are not electrically conductive until the oxide shell is broken or removed. In our FM-TPE composite system, due to the spacing between the NPs and the existence of the oxide shell on the NPs' surface, conductive pathways cannot be generated, and the composite will be electrically insulative in the as-printed state. For instance, the conductivity of the as-printed 80 wt % FM-TPE structure was measured to be 1.38×10^{-7} S/m (Figure 6A). Cross-section SEM (Figure 6B) confirms that FM NPs are dispersed in the polymer matrix without formation of interconnected metal structure. Different methods can be used to form conductive pathways in liquid metals or LMPAs.[63,64]

We first studied thermal annealing as a potential method to enhance the electrical conductivity of the FM-TPE composites. In the first method, we thermally annealed the as-printed sample at 120°C for 12 h. The electrical conductivity of the thermally annealed sample increased by about 6 orders of magnitude to 7.80×10^{-2} S/m

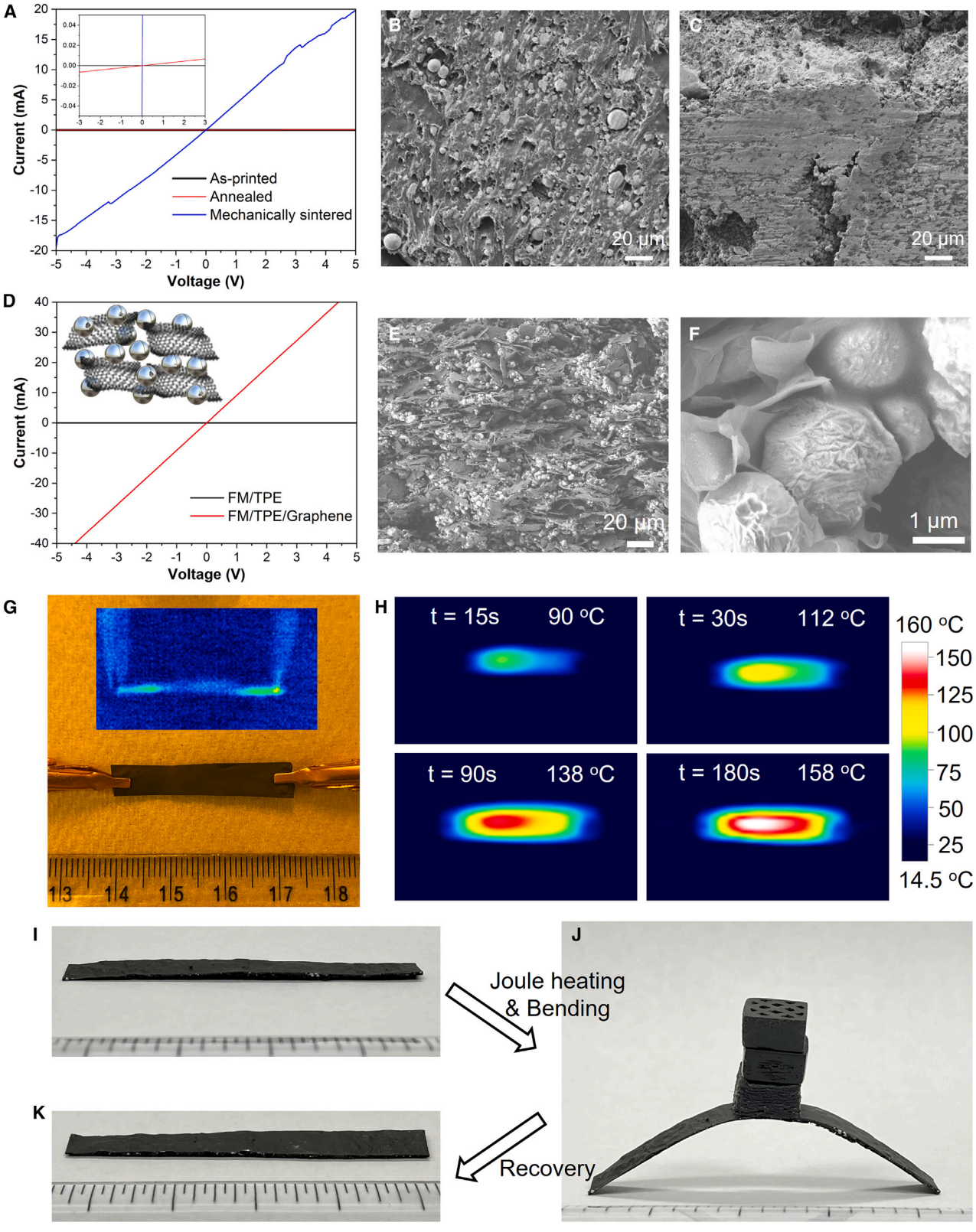

Figure 6. Transformation from insulative to conductive state and Joule heating-induced reversible shape changes

(A) Electrical conductivity of 3D-printed 80 wt % FM-TPE composite in as-printed, thermally annealed, and mechanically sintered states.

(B and C) Cross-section SEM images of the 80 wt % FM-TPE composite (B) in as-printed state and (C) after mechanically induced coalescence.

(D) Electrical conductivity of the FM-TPE-graphene composite; inset shows the schematic of the internal structure.

(E and F) Cross-section SEM images of the FM-TPE-graphene composite at two different magnifications.

(G) Photo of the FM-TPE-graphene composite for Joule heating measurements.

(H) IR imaging of the FM-TPE-graphene composite at different time points with increasing temperature.

(I–K) Reversible shape transformation of the FM-TPE-graphene composite (I) in the initial state and (J) after Joule heating and bending and (K) recovery to flat state after Joule heating and cooling. Scale bars, 20 μm (B, C, and E) and 1 μm (F).

(Figure 6A). The probable mechanism is that, during thermal annealing (above the T_g for the TPE matrix), the polymer chains in the TPE matrix relax and rearrange, and the FM NPs are also melted, so that more pronounced phase separation between FM and TPE in the matrix as well as local coalescence of FM NPs can occur.

To further enhance electrical conductivity, we conducted mechanically induced sintering on the 3D-printed FM-TPE composites. In this process, a stylus can be used to mechanically scribe along the surface of a heated sample (at 85°C), or the sample (for cylindrical shape) can be rolled between two rigid plates. The process is still non-destructive, as the force applied is within the elastic deformation range of the TPE matrix. The 80 wt % FM-TPE composite structure after mechanical sintering showed a dramatic increase (9 orders of magnitude) in conductivity to 2.78×10^2 S/m (Figure 6A). Cross-section SEM (Figure 6C) further confirmed that a large fraction of the FM NPs form a continuous metal structure after coalescence with a small fraction remaining discrete.

Both the thermal annealing and the mechanical sintering methods require post-printing processing to transform the composites into a highly conductive state, which is not desirable for some applications. To address this challenge, we incorporate graphene into the composites, which can bridge the adjacent FM NPs to enable high conductivity in the as-printed state. For instance, the FM-TPE-graphene composite (80 wt % FM and 10% graphene) shows an intrinsic high conductivity of 10^2 S/m (Figure 6D). Cross-section SEM images (Figure 6E) show that the 2D graphene nanosheets intercalated with the FM NPs into an organized internal structure. Interestingly, some of the FM NPs were wrapped with graphene sheets as indicated by the characteristic wrinkles on the surface (Figure 6F).

The high conductivity and ordered internal structure of the FM-TPE-graphene composites enable a strong Joule heating effect. We studied this by applying a 15 V voltage across a rectangle-shaped FM-TPE-graphene composite and monitoring the temperature rise with an infrared (IR) camera (Figure 6G). The temperature of the sample (Figure 6H) quickly increased to 112°C at 30 s and 158°C at 180 s. These temperatures are higher than the T_g of TPE and T_m of the FM NPs, so that the composite structure also softens substantially during the Joule heating process.

The reversible mechanical property changes during Joule heating can be utilized to achieve reversible and programmable shape transformations. We demonstrated this by using a rectangular FM-TPE-graphene composite (Figures 6I–6K). The structure was flat in the initial state, and after application of a 15 V voltage for 30 s, it softened and could be easily shaped into desirable geometries such as an arc shape (Figure 6J). The bent shape can be stably fixed by pausing the voltage, so that the FM NPs solidify, and the overall structure becomes rigid. The arc-shaped structure can withstand more than 20 times its own weight without deformation. Subsequently, to recover its original shape (Figure 6K), the electrical voltage can be applied again to soften the structure and enable a full recovery.

Theoretical and experimental study on mechanical properties

The incorporation of metal NPs in a TPE matrix is expected to have a substantial effect on the mechanical properties of the composites and 3D-printed structures. Theoretical investigation using coarse-grained molecular dynamics (MD) modeling was conducted on the composites. This model adopts a discretized triangular spring network and mass beads at the network nodes for the composite mechanics and mass. The mechanical parameters of FM springs and TPE springs are determined by Young's modulus and the strength of these materials measured experimentally, and their spatial distribution is determined according to the results of the phase-field simulations.

We theoretically studied the effects of FM content on the mechanical properties of the FM-TPE composites (Figure 7A, see also Table S3). From the stress-strain curves, it can be seen that, with the increase in FM content, the modulus gradually increases, the ultimate strength has a slight decrease, and the yield strain has a substantial decrease. It is noted that all curves show a long tail at high strain, which is due to the existence of soft/polymer bridges that still connect the sample after the rigid regions are broken. When the FM content increased to 95 wt %, a continuous metal network spontaneously formed, and the modulus was significantly increased to a value (E = 2.2 GPa) that was close to that of FM and significantly higher than that of composites with lower FM content (Table S3). The internal structures of those composites right before rupture are shown in Figure 7B. It shows that the microcracks are formed at or close to the interface between the metal and the polymer matrix. Also, with increasing FM content in the composites, the number of microcracks is reduced and the size of the microcracks is increased.

We also studied the effects of internal structure on the mechanical properties of FM-TPE composite at a fixed composition; the results are shown in Figures 7C and 7D. For the 70 wt % FM-TPE composite, the metal phase is composed of discrete NPs in the TPE matrix, and the four different initial states (insets in Figure 6C) correspond to increasing average NP size. The stress-strain curves were obtained by applying tensile stress to the coarse-grained MD model. The mechanical properties of composites with those different internal structures are very close to one another. The internal structures during crack initiation and rupture (Figure 7D) show that the microcracks are mainly initiated at the metal/polymer interface, and composites with a higher number of FM NPs have more microcracks with smaller size.

We then experimentally characterized the mechanical properties of FM-TPE filaments with tensile testing (Figure 7E and Table 1). The 10 wt % FM-TPE filament has a modulus of 380 MPa, tensile strength of 9.6 MPa, and elongation at break of 54.6%. With the increase in FM content, the FM-TPE filaments show increasing modulus, but at the cost of decreasing strength and elongation at break. The experimental tensile results match well with the coarse-grained MD simulation; the differences in quantitative values mainly originate from the size difference between the simulation box and the experimental samples, as well as defects during sample preparation.

The FM-TPE filaments were used to 3D print dog bone samples for tensile testing (Figure 7F). For instance, at ambient temperature (25°C), the 3D-printed 70 wt % FM-TPE shows a modulus of 612 MPa, strength of 8.5 MPa, and elongation at break of 18.4% (Table 1). Those values are substantially higher than that of the corresponding filament, which is unique and advantageous for fabricating stable and strong 3D composite structures. The probable reason for such enhancement is that during the

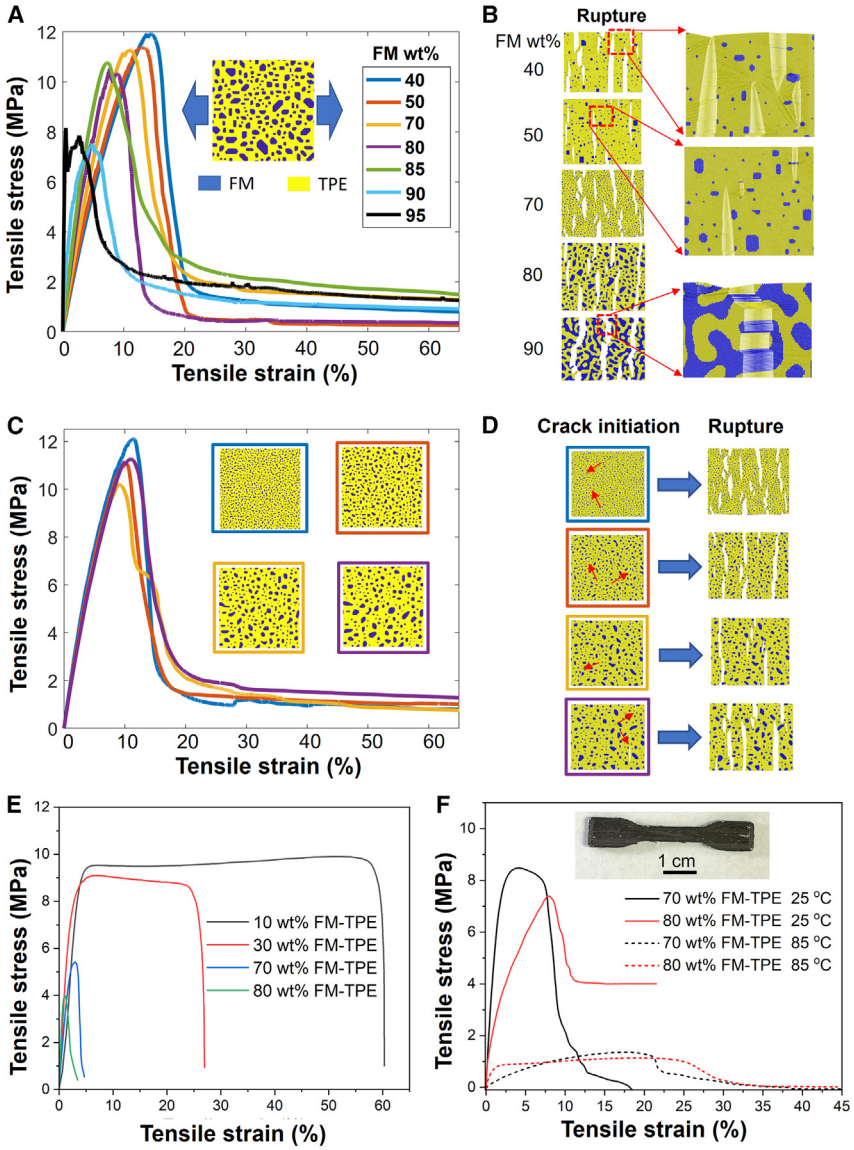

Figure 7. Mechanical properties of the FM-TPE composites and 3D-printed structures from computational modeling and experiments

(A) Stress-strain curves for FM-TPE composites with different FM contents from coarse-grained MD simulation.

(B) Internal structures of the FM-TPE composites right before rupture.

(C) Stress-strain curves for 70 wt % FM-TPE with different initial internal structures based on phase-field simulation; curves with different colors correspond to the different inset morphologies.

(D) Snapshots of the 70 wt % FM-TPE composites with different internal structures during crack formation and rupture. The size of all the simulation boxes in their initial state is 75 μm.

(E) Stress-strain curves for FM-TPE filaments with 10, 30, 70, and 80 wt % FM in experiments.

(F) Stress-strain curves for 3D-printed dog bones with 70 and 80 wt % FM at two different temperatures in experiments. Inset shows a representative photo of a 3D-printed dog bone, and the scale bar represents 1 cm.

FFF 3D printing, the composites were melt-extruded from the nozzle, during which the two-phase structures can evolve into more stable configurations through rearrangement and coalescence of FM NPs.

Table 1. Mechanical properties by tensile testing of FM-TPE composites

Composition	Sample state	Tensile strength (MPa)	Elongation at break (%)	Modulus (MPa)
10 wt % FM-TPE	filament	9.6 ± 0.2	54.6 ± 5.4	380 ± 56
30 wt % FM-TPE	filament	9.3 ± 0.6	24.3 ± 3.5	428 ± 40
70 wt % FM-TPE	filament	4.9 ± 0.4	5.1 ± 0.6	431 ± 29
80 wt % FM-TPE	filament	4.0 ± 0.1	3.9 ± 0.4	651 ± 55
70 wt % FM-TPE	3DP dog bone	8.5 ± 0.3	18.4 ± 1.1	612 ± 32
80 wt % FM-TPE	3DP dog bone	8.0 ± 0.2	19.0 ± 1.3	790 ± 41

Importantly, due to the reversible phase transition of FM NPs at their melting point (62°C), the 3D-printed structures are expected to have significantly different mechanical properties at temperatures below and above that transition. This was confirmed by tensile testing of the 3D-printed FM-TPE at 85°C (Figure 7F), which shows a much lower modulus of 22 MPa, a strength of 1.3 MPa, and an increased elongation at break close to 40%. Similar strong temperature dependence of mechanical properties was also observed for the 3D-printed 80 wt % FM-TPE sample, whose modulus decreased from 790 MPa at 25°C to 98 MPa at 85°C. The TPE matrix also has temperature-dependent mechanical properties (Figure S6), but their extent is much lower than that of the FM-TPE composites. Such reversible and temperature-dependent mechanical properties will be useful for applications in soft actuators and robotics.

Additive manufacturing of polymers and metals is usually achieved with very different and incompatible methods and conditions. In this work, by integrating LMPA, TPE, and graphene into functional composites with widely tunable structures and properties, we have achieved 3D-printable polymer-metal composites that are fully compatible with the widely used FFF method. The processing-structure-property relationship and 3D printability of such FM-TPE composites were elucidated by systematic characterization and multiphysics modeling. The FM NP loading in the TPE matrix has significant effects on the printing and physical properties of the 3D-printed structures. At relatively low FM content, the FM NPs remain separated in the TPE matrix and the overall composite structures are soft and electrically insulative. At high FM content (80 wt % or higher), the composites are much more rigid, and conductive pathways in the TPE matrix can be achieved by inducing the coalescence between adjacent FM NPs with thermal and/or mechanical methods. The reversible melting-solidification of FM NPs in a soft matrix also enables the on-demand and reversible tuning of the mechanical properties of the composite structures. Importantly, the 3D-printed FM-TPE composites can be conveniently recycled into their original components by solvent treatment and reused for new 3D printing.

Moreover, the incorporation of graphene can effectively bridge the adjacent FM NPs and significantly enhance the electrical and thermal conductivity of the FM-TPE composites and 3D-printed structures. Also, the interpenetrated metal-graphene network enables excellent shape retention after removing the TPE with calcination, so that 3D metal-graphene structures with well-defined sizes and shapes can be conveniently fabricated. A strong Joule heating effect of the 3D-printable FM-TPE-graphene composites was also demonstrated, and such rapid temperature increase was accompanied by the significant softening of the composites due to the melting of FM and reaching the rubbery state of the TPE. Reversible and programmable shape transformation of the FM-TPE-graphene composites was achieved by taking advantage of the reversible softening and solidification of the composites

with electrical voltage. Our study provides a versatile material platform for additive manufacturing of polymer-metal and metal-graphene composites and has promising applications in soft electronic sensors, robotics, and energy storage.

EXPERIMENTAL PROCEDURES

Resource availability

Lead contact

Further information and requests for resources should be directed to and will be fulfilled by the lead contact, Weinan Xu (weinanxu@uakron.edu).

Materials availability

All composites can be produced according to the procedures outlined below from commercial reagents.

Data and code availability

All experimental and simulation data are available upon request from the lead contact.

Materials

FM (Roto144F low-melt fusible ingot alloy) was purchased from Rotometals. PS (MW 192,000 g/mol) and 1-dodecanethiol were purchased from Sigma-Aldrich. SIBS (SIBSTAR 073T, MW 75,500 g/mol) was received from Kaneka. Toluene was purchased from Fisher Scientific. Graphene was prepared by electrochemical exfoliation of graphite. All chemicals were used as received without any purification unless otherwise clarified.

Fabrication of FM NPs

Bulk FM pieces with measured weight were cut and placed in toluene with the addition of organic ligand 1-dodecanethiol. The solution was then heated to 80°C and probe sonicated (QSONICA Q55) for 10 min. The particle size can be controlled within a range by the sonication time and amplitude. The organic ligands help to stabilize the FM NPs and prevent aggregation. The produced FM NPs were collected by centrifugation and washed with toluene three times to remove the excess thiol ligand.

Fabrication of FM-TPE composite filaments

In a typical procedure, SIBS copolymer and PS homopolymer (weight ratio 1:1) were dissolved in toluene to get 2 wt % polymer solution. Then a corresponding amount of FM based on the required weight fraction was added to the polymer solution, together with 1-dodecanethiol ligand. The solution was then heated to 85°C to melt the FM, and two cycles of probe sonication (15 min each with 10 min interval) were used to disperse the FM NPs homogeneously in the polymer solution. Subsequently, the solution was transferred to a polytetrafluoroethylene (PTFE) mold and slightly heated (40°C) until the solvent was fully evaporated. The composite film was then cut into small pieces and fed into a desktop extruder (Wellzoom B2) to fabricate the filament. The extruding temperature was set at 170°C, and the diameter of the extrusion nozzle was 1.75 mm. Filaments were cooled in air and collected. The rate of filament production was 2–5 mm/s.

FFF 3D printing

FM-TPE composite filaments were used for FFF 3D printing by a commercial 3D printer (Wanhao Duplicator i3) equipped with a modified printing head (Flexion extruder). The nozzle diameter was 0.8 mm, the printing temperature was 230°C, the build plate temperature was 60°C, and the printing rate could be varied from

2 to 20 mm/s. The printing head moved in x, y, and z directions controlled by the software. Three-dimensional models were built using SolidWorks software.

Recycling of the 3D-printed structures

The 3D-printed composite structure was immersed in toluene to dissolve the TPE matrix. Then the solution was centrifuged to separate the FM NPs from the polymer solution (7,000 rpm for 5 min). The supernatant was transferred to a PTFE dish and dried to obtain the TPE polymer film. The precipitated FM NPs were collected and washed. Then the FM NPs were placed in 1 M HCl and heated above the T_m to fuse them together into a bulk piece, followed by DI water washing and drying.

Characterization

Atomic force microscopy (AFM) was conducted with a Bruker Dimension Icon AFM. Images were acquired in tapping mode using Si cantilevers with 300 kHz resonance frequency at 0.5 Hz scan rate. SEM was conducted using a JEOL-7401 FE-SEM at 5 kV accelerating voltage. Rheological properties were studied with a capillary rheometer (Rosand RH 7) at 230°C. The shear rate was set in the 5–1,000 s^{-1} range. A die with a 24:1 L/D ratio and 1 mm diameter was used. Thermal stability was studied by TGA (TA Instruments Q500). The temperature range was from room temperature to 700°C at a heating rate of 10°C min^{-1}. The experiment was conducted under a nitrogen atmosphere. DMA (TA Q800) was used to characterize the viscoelastic behavior in the −100°C to 120°C range. The heating and cooling rate was 5°C min^{-1}. Samples were oscillated at 1.0% strain amplitude at 1 Hz frequency. Tensile tests were conducted with an Instron 4204 tensile tester according to the ISO 37 standard. The electrical conductivity was measured by the two-probe method using a Keithley 2400 source meter. Sweep mode was utilized with a measuring window from −5 to 5 V. The IR thermal imaging was conducted with a Testo 870 thermal imaging camera. Micro-CT scan was conducted on a Bruker Skyscan 1172; the voltage was set at 80 kV, the X-ray source current was 124 μA, and the exposure time was 646 ms for each rotation step.

Phase-field model

A phase-field model was used to simulate the diffusion and separation of the binary FM-TPE melt mixture, which enabled the two melts to start with arbitrary mixed conformation and form an equilibrated structure. This model is enabled by numerically solving the Cahn-Hilliard equation given as:

$$\frac{\partial u}{\partial t} = \nabla^2\left[\frac{df(u)}{du} - \theta^2\nabla^2 u\right], \qquad \text{(Equation 1)}$$

where $-1 < u < 1$ is the difference in concentration of the two phases ($u < 0$ for TPE and $u \geq 0$ for FM), $f(u) = \frac{1}{4}(u^2 - 1)^2$ is the double-well free-energy function, and θ is the width of transition region between the two phases, in analogy to a diffusion coefficient with a unit of $[length]^2/\sqrt{[time]}$. The discretized form of this differential equation with periodic boundary conditions in the x–y direction enables simulating the time evolution of the two mixed phases in the 2D plane.

Coarse-grained molecular dynamics model

We use a coarse-grained model composed of a regular triangular meshwork to model the FM-TPE composite. Each spring is modeled by a Morse potential. The spring energy is given by:

$$E = D\left[1 - e^{-\alpha(r-a)}\right]^2, \qquad \text{(Equation 2)}$$

where D and α are parameters of the potential energy, and a is initial length of the spring that corresponds to the lattice constant of the triangular network. Considering

the area of each mass bead, as the node of the network, is given by $\frac{\sqrt{3}}{2}a^2$, and each bead is connected to three neighboring beads, the spring stiffness is given by:

$$\frac{d^2E}{dr^2}(r = a) = 2D\alpha^2 = \frac{\sqrt{3}}{4}Et, \quad \text{(Equation 3)}$$

where E is Young's modulus and t is the material thickness. The spring strength is given by:

$$max\left(\frac{dE}{dr}\right) = \frac{1}{2}D\alpha = \frac{\sqrt{3}}{3}\sigma_c ta, \quad \text{(Equation 4)}$$

where σ_c is the material ultimate strength. Using Equations 3 and 4, we can solve for the potential parameters as:

$$\alpha = \frac{3E}{16\sigma_c a} \text{ and } D = \frac{32\sqrt{3}}{9}\sigma_c^2 a^2 t \Big/ E. \quad \text{(Equation 5)}$$

We summarize the numerical value of the potential parameters of the two material phases (FM and TPE) in Table S2.

Multiphysics modeling

We use the phase-field model to generate the equilibrated structure with certain FM wt % and use the coarse-grained model to model the mechanics of each material phase. This model enables us to compare the deformation and failure mechanisms of the FM-TPE composites by adjusting the wt % and NP size as well as the phase mechanics and their interfacial strength. The simulations are performed by using a LAMMPS package[65] with time step of 0.01 μs and loading applied with a constant strain rate (0.0001/μs) under control.

SUPPLEMENTAL INFORMATION

Supplemental information can be found online at https://doi.org/10.1016/j.xcrp.2023.101604.

ACKNOWLEDGMENTS

W.X. gratefully acknowledges the startup support from the University of Akron. This work is also partially supported by the National Science Foundation (award no. 2213054). Z.Q. acknowledges a National Science Foundation CAREER grant (CMMI-2145392) and Collaboration for Unprecedented Success and Excellence (CUSE) at Syracuse University for supporting the research work. The authors thank Dr. Kevin Cavicchi and Dr. James Eagan for helpful discussion. We also would like to thank Kaneka Co. for providing the SIBS sample.

AUTHOR CONTRIBUTIONS

W.X. conceived and supervised the project; J.B. and N.S. performed the experimental study; Z.Q. performed the theoretical modeling; W.X., J.B., and Z.Q. wrote the manuscript.

DECLARATION OF INTERESTS

W.X. and J.B. are inventors on a patent application (USPTO: 63/464,782).

Received: June 13, 2023
Revised: August 5, 2023
Accepted: September 7, 2023
Published: September 29, 2023

REFERENCES

1. Truby, R.L., and Lewis, J.A. (2016). Printing soft matter in three dimensions. Nature *540*, 371–378. https://doi.org/10.1038/nature21003.

2. Valentine, A.D., Busbee, T.A., Boley, J.W., Raney, J.R., Chortos, A., Kotikian, A., Berrigan, J.D., Durstock, M.F., Lewis, J.A., Valentine, A.D., et al. (2017). Hybrid 3D printing of soft electronics. Adv. Mater. *29*, 1703817. https://doi.org/10.1002/ADMA.201703817.

3. Tumbleston, J.R., Shirvanyants, D., Ermoshkin, N., Januszewicz, R., Johnson, A.R., Kelly, D., Chen, K., Pinschmidt, R., Rolland, J.P., Ermoshkin, A., et al. (2015). Continuous liquid interface production of 3D objects. Science *347*, 1349–1352. https://doi.org/10.1126/science.aaa2397.

4. Das, S., Bourell, D.L., and Babu, S.S. (2016). Metallic materials for 3D printing. MRS Bull. *41*, 729–741. https://doi.org/10.1557/MRS.2016.217.

5. Khairallah, S.A., Martin, A.A., Lee, J.R.I., Guss, G., Calta, N.P., Hammons, J.A., Nielsen, M.H., Chaput, K., Schwalbach, E., Shah, M.N., et al. (2020). Controlling interdependent meso-nanosecond dynamics and defect generation in metal 3D printing. Science *368*, 660–665. https://doi.org/10.1126/SCIENCE.AAY7830.

6. Lee, J.Y.K., Pierce, J.T., Zeh, R., Cho, S.S., Salinas, R., Nie, S., and Singhal, S. (2017). Fundamentals and applications of 3D printing for novel materials. World Neurosurg. *106*, 120–130. https://doi.org/10.1016/J.APMT.2017.02.004.

7. Ngo, T.D., Kashani, A., Imbalzano, G., Nguyen, K.T., and Hui, D. (2018). Additive manufacturing (3D printing): A review of materials, methods, applications and challenges. Compos. B Eng. *143*, 172–196. https://doi.org/10.1016/J.COMPOSITESB.2018.02.012.

8. Giannopoulos, A.A., Mitsouras, D., Yoo, S.J., Liu, P.P., Chatzizisis, Y.S., and Rybicki, F.J. (2016). Applications of 3D printing in cardiovascular diseases. Nat. Rev. Cardiol. *13*, 701–718. https://doi.org/10.1038/nrcardio.2016.170.

9. Ambrosi, A., and Pumera, M. (2016). 3D-printing technologies for electrochemical applications. Chem. Soc. Rev. *45*, 2740–2755. https://doi.org/10.1039/C5CS00714C.

10. Ligon, S.C., Liska, R., Stampfl, J., Gurr, M., and Mülhaupt, R. (2017). Polymers for 3D printing and customized additive manufacturing. Chem. Rev. *117*, 10212–10290. https://doi.org/10.1021/acs.chemrev.7b00074.

11. Valino, A.D., Dizon, J.R.C., Espera, A.H., Chen, Q., Messman, J., and Advincula, R.C. (2019). Advances in 3D printing of thermoplastic polymer composites and nanocomposites. Prog. Polym. Sci. *98*, 101162. https://doi.org/10.1016/J.PROGPOLYMSCI.2019.101162.

12. Shen, N., Duan, L., Yang, M., Liu, S., and Xu, W. (2022). Solvent-assisted 3D printing of butyl rubber and its hybrid materials. MRS Commun. *12*, 597–602. https://doi.org/10.1557/s43579-022-00205-5.

13. Jiang, Z., Erol, O., Chatterjee, D., Xu, W., Hibino, N., Romer, L.H., Kang, S.H., and Gracias, D.H. (2019). Direct ink writing of poly(tetrafluoroethylene) (PTFE) with tunable mechanical properties. ACS Appl. Mater. Interfaces *11*, 28289–28295. https://doi.org/10.1021/acsami.9b07279.

14. Jiang, Z., Diggle, B., Tan, M.L., Viktorova, J., Bennett, C.W., and Connal, L.A. (2020). Extrusion 3D printing of polymeric materials with advanced properties. Adv. Sci. *7*, 202001379. https://doi.org/10.1002/advs.202001379.

15. Brenken, B., Barocio, E., Favaloro, A., Kunc, V., and Pipes, R.B. (2018). Fused filament fabrication of fiber-reinforced polymers: A review. Addit. Manuf. *21*, 1–16. https://doi.org/10.1016/j.addma.2018.01.002.

16. Gan, Z., Kafka, O.L., Parab, N., Zhao, C., Fang, L., Heinonen, O., Sun, T., and Liu, W.K. (2021). Universal scaling laws of keyhole stability and porosity in 3D printing of metals. Nat. Commun. *12*, 2379. https://doi.org/10.1038/s41467-021-22704-0.

17. Todaro, C.J., Easton, M.A., Qiu, D., Zhang, D., Bermingham, M.J., Lui, E.W., Brandt, M., StJohn, D.H., and Qian, M. (2020). Grain structure control during metal 3D printing by high-intensity ultrasound. Nat. Commun. *11*, 142–149. https://doi.org/10.1038/s41467-019-13874-z.

18. Visser, C.W., Pohl, R., Sun, C., Römer, G.W., Huis in 't Veld, B., Lohse, D., Sun, C., Lohse, D., Pohl, R., Römer, G., et al. (2015). Toward 3D printing of pure metals by laser-induced forward transfer. Adv. Mater. *27*, 4087–4092. https://doi.org/10.1002/ADMA.201501058.

19. Fafenrot, S., Grimmelsmann, N., Wortmann, M., and Ehrmann, A. (2017). Three-dimensional (3D) printing of polymer-metal hybrid materials by fused deposition modeling. Materials *10*, 1199. https://doi.org/10.3390/MA10101199.

20. Carrico, J.D., Traeden, N.W., Aureli, M., and Leang, K.K. (2015). Fused filament 3D printing of ionic polymer-metal composites (IPMCs). Smart Mater. Struct. *24*, 125021. https://doi.org/10.1088/0964-1726/24/12/125021.

21. Laureto, J., Tomasi, J., King, J.A., and Pearce, J.M. (2017). Thermal properties of 3D printed polylactic acid-metal composites. Prog. Addit. Manuf. *2*, 57–71. https://doi.org/10.1007/S40964-017-0019-X.

22. Ait-Mansour, I., Kretzschmar, N., Chekurov, S., Salmi, M., and Rech, J. (2020). Design-dependent shrinkage compensation modeling and mechanical property targeting of metal FFF. Prog. Addit. Manuf. *5*, 51–57. https://doi.org/10.1007/S40964-020-00124-8.

23. Alkindi, T., Alyammahi, M., Susantyoko, R.A., and Atatreh, S. (2021). The effect of varying specimens' printing angles to the bed surface on the tensile strength of 3D-printed 17-4PH stainless-steels via metal FFF additive manufacturing. MRS Commun. *11*, 310–316. https://doi.org/10.1557/S43579-021-00040-0.

24. Gibson, M.A., Mykulowycz, N.M., Shim, J., Fontana, R., Schmitt, P., Roberts, A., Ketkaew, J., Shao, L., Chen, W., Bordeenithikasem, P., et al. (2018). 3D printing metals like thermoplastics: Fused filament fabrication of metallic glasses. Mater. Today *21*, 697–702. https://doi.org/10.1016/J.MATTOD.2018.07.001.

25. Daeneke, T., Khoshmanesh, K., Mahmood, N., de Castro, I.A., Esrafilzadeh, D., Barrow, S.J., Dickey, M.D., and Kalantar-Zadeh, K. (2018). Liquid metals: Fundamentals and applications in chemistry. Chem. Soc. Rev. *47*, 4073–4111. https://doi.org/10.1039/c7cs00043j.

26. Dickey, M.D. (2017). Stretchable and soft electronics using liquid metals. Adv. Mater. *29*, 1606425. https://doi.org/10.1002/ADMA.201606425.

27. Khoshmanesh, K., Tang, S.Y., Zhu, J.Y., Schaefer, S., Mitchell, A., Kalantar-Zadeh, K., and Dickey, M.D. (2017). Liquid metal enabled microfluidics. Lab Chip *17*, 974–993. https://doi.org/10.1039/C7LC00046D.

28. Yan, J., Malakooti, M.H., Lu, Z., Wang, Z., Kazem, N., Pan, C., Bockstaller, M.R., Majidi, C., and Matyjaszewski, K. (2019). Solution processable liquid metal nanodroplets by surface-initiated atom transfer radical polymerization. Nat. Nanotechnol. *14*, 684–690. https://doi.org/10.1038/s41565-019-0454-6.

29. Thelen, J., Dickey, M.D., and Ward, T. (2012). A study of the production and reversible stability of EGaIn liquid metal microspheres using flow focusing. Lab Chip *12*, 3961–3967. https://doi.org/10.1039/C2LC40492C.

30. Tang, S.Y., Joshipura, I.D., Lin, Y., Kalantar-Zadeh, K., Mitchell, A., Khoshmanesh, K., and Dickey, M.D. (2016). Liquid-metal microdroplets formed dynamically with electrical control of size and rate. Adv. Mater. *28*, 604–609. https://doi.org/10.1002/ADMA.201503875.

31. Martin, A., Du, C., Chang, B., and Thuo, M. (2020). Complexity and opportunities in liquid metal surface oxides. Chem. Mater. *32*, 9045–9055. https://doi.org/10.1021/ACS.CHEMMATER.0C02047.

32. Lin, Y., Genzer, J., Dickey, M.D., Lin, Y., Genzer, J., and Dickey, M.D. (2020). Attributes, fabrication, and applications of gallium-based liquid metal particles. Adv. Sci. *7*, 2000192. https://doi.org/10.1002/ADVS.202000192.

33. Dong, C., Leber, A., Das Gupta, T., Chandran, R., Volpi, M., Qu, Y., Nguyen-Dang, T., Bartolomei, N., Yan, W., and Sorin, F. (2020). High-efficiency super-elastic liquid metal based triboelectric fibers and textiles. Nat. Commun. *11*, 3537–3539. https://doi.org/10.1038/s41467-020-17345-8.

34. Gao, J.Y., Chen, S., Liu, T.Y., Ye, J., and Liu, J. (2021). Additive manufacture of low melting point metal porous materials: Capabilities, potential applications and challenges. Mater. Today *49*, 201–230. https://doi.org/10.1016/J.MATTOD.2021.03.019.

35. Zhang, W., Chen, J., Li, X., and Lu, Y. (2020). Liquid metal-polymer microlattice metamaterials with high fracture toughness and damage recoverability. Small *16*, 2004190. https://doi.org/10.1002/SMLL.202004190.

36. Deng, F., Nguyen, Q.K., and Zhang, P. (2020). Multifunctional liquid metal lattice materials through hybrid design and manufacturing. Addit. Manuf. *33*, 101117. https://doi.org/10.1016/J.ADDMA.2020.101117.

37. Wang, L., and Liu, J. (2014). Compatible hybrid 3D printing of metal and nonmetal inks for direct manufacture of end functional devices. Sci. China Technol. Sci. *57*, 2089–2095. https://doi.org/10.1007/S11431-014-5657-3.

38. Neumann, T.V., Facchine, E.G., Leonardo, B., Khan, S., and Dickey, M.D. (2020). Direct write printing of a self-encapsulating liquid metal–silicone composite. Soft Matter *16*, 6608–6618. https://doi.org/10.1039/D0SM00803F.

39. Malakooti, M.H., Bockstaller, M.R., Matyjaszewski, K., and Majidi, C. (2020). Liquid metal nanocomposites. Nanoscale Adv. *2*, 2668–2677. https://doi.org/10.1039/d0na00148a.

40. Khondoker, M.A.H., Ostashek, A., and Sameoto, D. (2019). Direct 3D printing of stretchable circuits via liquid metal co-extrusion within thermoplastic filaments. Adv. Eng. Mater. *21*, 1900060. https://doi.org/10.1002/ADEM.201900060.

41. Markvicka, E.J., Bartlett, M.D., Huang, X., and Majidi, C. (2018). An autonomously electrically self-healing liquid metal–elastomer composite for robust soft-matter robotics and electronics. Nat. Mater. *17*, 618–624. https://doi.org/10.1038/s41563-018-0084-7.

42. Rich, S., Jang, S.H., Park, Y.L., and Majidi, C. (2017). Liquid metal-conductive thermoplastic elastomer integration for low-voltage stiffness tuning. Adv. Mater. Technol. *2*, 1700179. https://doi.org/10.1002/admt.201700179.

43. Shamberger, P.J., and Bruno, N.M. (2020). Review of metallic phase change materials for high heat flux transient thermal management applications. Appl. Energy *258*, 113955. https://doi.org/10.1016/J.APENERGY.2019.113955.

44. Çınar, S., Tevis, I.D., Chen, J., and Thuo, M. (2016). Mechanical fracturing of core-shell undercooled metal particles for heat-free soldering. Sci. Rep. *6*, 21864. https://doi.org/10.1038/srep21864.

45. Li, Z., Tevis, I.D., Oyola-Reynoso, S., Newcomb, L.B., Halbertsma-Black, J., Bloch, J.-F., and Thuo, M. (2015). Melt-and-mold fabrication (MnM-Fab) of reconfigurable low-cost devices for use in resource-limited settings. Talanta *145*, 20–28. https://doi.org/10.1016/j.talanta.2015.05.002.

46. Idrus-Saidi, S.A., Tang, J., Ghasemian, M.B., Yang, J., Han, J., Syed, N., Daeneke, T., Abbasi, R., Koshy, P., O'Mullane, A.P., and Kalantar-Zadeh, K. (2019). Liquid metal core–shell structures functionalised via mechanical agitation: the example of Field's metal. J. Mater. Chem. *7*, 17876–17887. https://doi.org/10.1039/C9TA05200C.

47. Tevis, I.D., Newcomb, L.B., and Thuo, M. (2014). Synthesis of liquid core-shell particles and solid patchy multicomponent particles by shearing liquids into complex particles (SLICE). Langmuir *30*, 14308–14313. https://doi.org/10.1021/la5035118.

48. Jeyakumar, M., Hamed, M., and Shankar, S. (2011). Rheology of liquid metals and alloys. J. Nonnewton. Fluid Mech. *166*, 831–838. https://doi.org/10.1016/J.JNNFM.2011.04.014.

49. Spontak, R.J., and Patel, N.P. (2000). Thermoplastic elastomers: fundamentals and applications. Curr. Opin. Colloid Interface Sci. *5*, 333–340. https://doi.org/10.1016/S1359-0294(00)00070-4.

50. Puskas, J.E., and Kaszas, G. (1996). Polyisobutylene-based thermoplastic elastomers: A review. Rubber Chem. Technol. *69*, 462–475. https://doi.org/10.5254/1.3538381.

51. Shen, N., Liu, S., Kasbe, P., Khabaz, F., Kennedy, J.P., and Xu, W. (2021). Macromolecular engineering and additive manufacturing of poly(styrene-b-isobutylene-b-styrene). ACS Appl. Polym. Mater. *3*, 4554–4562. https://doi.org/10.1021/ACSAPM.1C00616.

52. Shen, N., Bu, J., Prévôt, M.E., Hegmann, T., Kennedy, J.P., Xu, W., Shen, N., Bu, J., Kennedy, J.P., and Xu, W. (2023). Macromolecular engineering and additive manufacturing of polyisobutylene-based thermoplastic elastomers. II. the poly(styrene-b-isobutylene-b-styrene)/poly(phenylene oxide) system. Macromol. Rapid Commun. *44*, 2200109. https://doi.org/10.1002/MARC.202200109.

53. Okatenko, V., Castilla-Amorós, L., Stoian, D.C., Vávra, J., Loiudice, A., and Buonsanti, R. (2022). The Native Oxide Skin of Liquid Metal Ga Nanoparticles Prevents Their Rapid Coalescence during Electrocatalysis. J. Am. Chem. Soc. *144*, 10053–10063. https://doi.org/10.1021/jacs.2c03698.

54. Hafiz, S.S., Labadini, D., Riddell, R., Wolff, E.P., Xavierselvan, M., Huttunen, P.K., Mallidi, S., and Foster, M. (2020). Surfaces and Interfaces of Liquid Metal Core–Shell Nanoparticles under the Microscope. Part. Part. Syst. Char. *37*, 1900469. https://doi.org/10.1002/ppsc.201900469.

55. Martin, A., Chang, B.S., Pauls, A.M., Du, C., and Thuo, M. (2021). Stabilization of Undercooled Metals via Passivating Oxide Layers. Angew. Chem. Int. Ed. *60*, 5928–5935. https://doi.org/10.1002/anie.202013489.

56. Ma, J., and Zhang, P. (2021). Supercooling suppression of phase change liquid metal–polydimethylsiloxane soft composites. Mater. Adv. *2*, 7437–7444. https://doi.org/10.1039/d1ma00601k.

57. Sun, X.Y., Xu, G.K., Li, X., Feng, X.Q., and Gao, H. (2013). Mechanical properties and scaling laws of nanoporous gold. J. Appl. Phys. *113*, 23505. https://doi.org/10.1063/1.4774246/924703.

58. Cahn, J.W., Hilliard, J.E., Chem Phys, J., Carn A, J.W., and John Hilliard, D.E. (1958). Free energy of a nonuniform system. I. interfacial free energy. J. Chem. Phys. *28*, 258–267. https://doi.org/10.1063/1.1744102.

59. Rizos, A.K., Ngai, K.L., and Plazek, D.J. (1997). Local segmental and sub-Rouse modes in polyisobutylene by photon correlation spectroscopy. Polymer *38*, 6103–6107. https://doi.org/10.1016/S0032-3861(97)00188-2.

60. Suleiman, D., Padovani, A.M., Negrõn, A.A., Sloan, J.M., Napadensky, E., and Crawford, D.M. (2014). Mechanical and chemical properties of poly(styrene-isobutylene-styrene) block copolymers: Effect of sulfonation and counter ion substitution. J. Appl. Polym. Sci. *131*, 40344. https://doi.org/10.1002/app.40344.

61. Kalathi, J.T., Grest, G.S., and Kumar, S.K. (2012). Universal viscosity behavior of polymer nanocomposites. Phys. Rev. Lett. *109*, 198301. https://doi.org/10.1103/PhysRevLett.109.198301.

62. Al-Mulla, A., and Gupta, R.K. (2000). Droplet coalescence in the shear flow of model emulsions. Rheol. Acta *39*, 20–25. https://doi.org/10.1007/s003970050003.

63. Wang, H., Yao, Y., He, Z., Rao, W., Hu, L., Chen, S., Lin, J., Gao, J., Zhang, P., Sun, X., et al. (2019). A Highly stretchable liquid metal polymer as reversible transitional insulator and conductor. Adv. Mater. *31*, 1901337. https://doi.org/10.1002/ADMA.201901337.

64. Chen, S., Wang, H.Z., Sun, X.Y., Wang, Q., Wang, X.J., Chen, L.B., Zhang, L.J., Guo, R., and Liu, J. (2019). Generalized way to make temperature tunable conductor–insulator transition liquid metal composites in a diverse range. Mater. Horiz. *6*, 1854–1861. https://doi.org/10.1039/C9MH00650H.

65. Plimpton, S. (1995). Fast parallel algorithms for short-range molecular dynamics. J. Comput. Phys. *117*, 1–19. https://doi.org/10.1006/JCPH.1995.1039.